Tutor/s

Dra. Maria Sarret Pons
Departament de Ciència de Materials i Química Física

Dr. Vicente Albaladejo Fuentes
Departament de Ciència de Materials i Química Física

Grau de Química

Treball Final de Grau

Anisotropic properties of additively manufactured components. Are they there?

Tenen propietats anisotròpiques els components fets per fabricació aditiva?

Lidia Fernández Vila

June 2021

Universitat de Barcelona

B:KC Barcelona Knowledge Campus
Campus d'Excel·lència Internacional

Nada en la vida debe ser temido, solamente comprendido. Ahora es el momento de comprender más, para temer menos.

Marie Curie

Primer de tot agrair als meus tutors Vicente Albaladejo i Maria Sarret tota l'ajuda, passió i predisposició mostrada al llarg d'aquest projecte, sense ells no hagués sigut el mateix. Tanmateix dono gràcies a aquest projecte per fer-me veure que el camp dels materials té molt camí encara per recórrer i animar-me a seguir formant-me per poder implicar-m'hi en un futur.

Gràcies també als amics que m'enduc d'aquesta etapa universitària, que tot i aquest darrer any de poca activitat, sempre han estat allà per donar suport i fer més fàcil qualsevol situació que se'ns presentés.

Finalment gràcies a la meva família i especialment a la meva mare, la dona més forta i valenta que conec, que sempre ens ha ensenyat que les coses no venen soles i que cadascú s'ho ha de guanyar treballant, amb esforç i ganes.

REPORT

CONTENTS

1. SUMMARY

In this project we have focused on studying the properties of a product manufactured by a coating technique known as Cold Gas Spray. This technique is differentiated from the others by the fact that it deposits the material in its solid form using kinetic energy to deform plastically the particles which lead to obtain a deposition. Since this technique is principally used in coatings, it results of high interest to prepare and characterize a component by this method with a significant volume in order to know the capabilities of this technique as an Additive Manufacturing process and to know the generation of anisotropic properties in the component.

First of all, it has been manufactured a high volume deposit from which it has been obtained two sample types: parallel (XZ) and perpendicular (XY) to spray direction. Afterwards, it has been analyzed the microstructure and porosity of both planes, as well as their corrosion resistance by using a Potentiodinamic Polarization. It has been also studied the mechanical properties of X, Y and Z directions via tensile test, and microhardness of XZ and XY planes with Vickers method.

It has been proved in all the performed tests that there is a clear anisotropy between XY and XZ planes, as well as between Z direction and X and Y directions. XZ plane has been the one that presented higher levels of porosity, lower corrosion and stress resistance and lower microhardness. That is due to its lamellar microstructure, which indicates low compaction and cohesion between layers in the sample.

Finally, samples have been thermally treated and it has been shown a considerable improvement in their properties, since they almost lose their anisotropic properties. However, they did not reach 316L Stainless Steel manufactured in a conventional manner.

Keywords: Cold Gas Spray, Additive Manufacturing, corrosion resistance, mechanical properties, anisotropic properties

2. RESUM

En aquest projecte ens hem centrat en estudiar les propietats que presenta un producte fabricat per una tècnica de recobriments anomenada Cold Gas Spray. Aquesta tècnica es diferencia de les demès pel fet que diposita el material en estat sòlid utilitzant l'energia cinètica per deformar plàsticament les partícules, fet que porta a obtenir un depòsit. Com és una tècnica principalment utilitzada en recobriments, és d'un alt interès preparar i caracteritzar un compost d'un volum apreciable fet per aquest mètode per conèixer la capacitat d'aquesta tècnica com a un procés de fabricació additiva i la generació de propietats anisotròpiques en el producte.

Primer de tot s'ha fabricat una deposició d'alt volum a partir de la qual s'ha obtingut dos tipus de mostres: paral·lela a la direcció de l'esprai (XZ) i perpendicular a aquesta (XY). Seguidament, s'ha analitzat la microestructura i porositat dels dos plans, així com la seva resistència a la corrosió mitjançant una Polarització Potenciodinàmica. S'ha estudiat també les propietats mecàniques de les direccions X, Y i Z amb l'assaig de tracció, i la microduresa dels plans XZ i XY amb el mètode de Vickers.

S'ha pogut comprovar en tots els assajos realitzats com hi ha una clara anisotropia entre els plans XY i XZ, així com també entre la direcció Z i les direccions X i Y. Essent el pla XZ el que presenta valors més alts de porositat, menys resistència a la corrosió i a la tracció i menys microduresa. Tot això és degut a la seva microestructura laminar, el que ens indica poca compactació i cohesió entre les capes de la mostra.

Per últim, s'han tractat tèrmicament les mostres i s'ha observat com les propietats milloren considerablement ja que gairebé perden les propietats anisotròpiques. Tot i això, no arriben a nivells d'un acer inoxidable 316L fet de la manera convencional.

Paraules clau: Cold Gas Spray, fabricació additiva, resistència a la corrosió, propietats mecàniques, propietats anisotròpiques.

3. INTRODUCTION

Additive Manufacturing (AM) or **Three-Dimensional Printing** (3D printing) was born in order to meet the needs and also innovate by improving the geometrical complexity of some products changing the way they are made. It is a manufacturing process in which the final object is made in an additive manner, that is, layer by layer[1]. On the basis of a digital three-dimensional model made by using special software or three-dimensional scanning, it is possible to divide the final component into individual layers and to stablish the path code for the printing machine.

After technology boom, AM has achieved an important position due to its capability to advanced design methodology (flexible design), variety on suitable materials, automate processing and equipment[2]. Since many materials can be suitable, we have decided to focus on **metal three-dimensional printing**, the main area where it is implemented is aerospace and automotive industry, among others, because of their requirements of strength and lightweight. Furthermore, it is also not unusual that application-oriented research is increasingly supported (functional printing)[3]; optimization of the speed and quality of the printing process are the main purpose as well as increasing the range of suitable metals. Presently, AM can be classified into four categories[4] according to the raw material nature used: liquid based, solid based, wire based and powder-based (Binder Jetting, Metal Powder Application, Powder Bed Fusion and Powder Direct Energy Deposition[5]). Powder Bed Fusion technology consists of manufacturing compounds by starting with a powder bed, which in different conditions is melted by a laser beam layer by layer while the support of the piece is going down and the next powder bed entering.

3.1. COLD GAS SPRAY

There are many methods related to surface engineering in order to prevent environmental corrosion, wear, high temperatures and chemical attack. One of them is **Thermal Spraying Technology**, where many materials are suitable to be used. The main thermal spray processes are: Flame Spray (FS), Arc Spray (AS), Plasma Spraying (PS) and High Velocity Oxy-Fuel

Spraying (HVOF)[6]. All of them consist of heating the material (powder or wire form) up to melting point and sprayed to a surface or substrate material, and then kinetic and thermal energy is transferred to the material.

According to the thermal spray process, spray parameters and feedstock material that we chose, we obtain different properties in coatings with different applications in transport, energy, biomedicine and electronics among others[7]. Thermal sprayed coatings have been produced for decades, but recently developments in these technologies have allowed producing high performance coatings of a great range of materials on many different substrates. This, it has been possible via improving spraying process controls, by using *state of the art* methods of feedstock materials production, and by using modern techniques of quality assurance.

In the middle eighties a new thermal sprayed coating method was developed: **Cold Gas Spray** (CGS)[8]. It differs from conventional thermal spray methods in the fact that it works well below the melting temperatures of the feedstock materials, making the process suitable for heat sensitive materials. In CGS, solid state powders are accelerated by a highly pressurized gas (typically nitrogen or helium) previously preheated and expanded in a converging/diverging *De Laval* type nozzle. Depending on the choice of spraying temperature and gas pressure, powder particles can reach velocities ranging from 200 to 1200 m/s and the particle temperature upon impact ranges between room temperature and 1000°C. This particle conditions allow performing a coating when they impact on the substrate.

3.1.1. Main parameters and bonding mechanism

The key parameters that determine CGS process and has to be established are the following[9]:

- **Impact particle velocity**: In order to produce particle deposition, particles should achieve a critical velocity to deform plastically when they impact on the substrate.
- **Spray angle of the gun**: Maximum deposition occurs when substrate and projection beam are perpendicular (90°), bellow this angle particle deposition decreases[10].
- **Stand-off distance**: Due to the effect wave from the previous particles impacting the substrate, the following lose speed during the spray process. For this reason medium

stand-off distance will be positive to avoid this effect and enable the deposition unhindered[11].

- **Substrate surface roughness**: As roughness in the substrate is high, the first layers of particles can have an additional compression degree, affecting the deposition efficiency.
- **Powder morphology and distribution**: Spherical morphology is the best to assure greater impact surface. Also narrow ranges of particle size distribution help to homogenize the impact energy and obtain better results in deposition.
- **Feeding rate**: It varies the coating thickness up to a maximum.
- **Particle and gas temperatures**: The higher the particle temperatures, the lower the critical speed.

Therefore, all these parameters need to be taken into account when we begin the process since they influence the deposition properties.

Bonding mechanism in CGS technology is not a chemical reaction between metal particles, there is a transformation of high kinetic energy into thermal[8] by experiencing **plastic deformation** of particles. This transformation of energy results into a viscous flow of the material to eliminate stress which promotes particle adhesion; the zone that experiences a better bonding is where shear stress is higher and it suffers a temperature rise: the interface between particle and substrate[12]. We can also appreciate different behavior depending on the substrate and particles strength[13] as well as depending on the section we observe, since it is not the same when particles bonding is seen from its perpendicular plane than from above, which can leads to anisotropic properties, described below.

Another aspect to take into account is the **critical particle velocity**[9,14] since below this value particles do not deform plastically and deposition cannot takes place. It is important also to work in the range of velocities above this critical velocity, where deposition efficiency is higher (this range is known as *window of deposition)* since if we exceed it, erosion occurs decreasing deposition efficiency.

Unlike other AM methods[6], CGS is remarkable for the absence of oxides in their products due to particles high velocity, rapid cohesion and solidification, which prevents from external contamination and formation of oxides that can influence anticorrosive, microstructural or

mechanical properties. Finally, due to its bonding mechanism described above and the additive manufacturing manner, the components obtained have **lamellar microstructure** associated with the previous variable parameters such as feedstock size or particle velocity.

3.1.2. Anisotropic properties

Another point to consider is the **anisotropic properties** acquired, in other words, its properties depend on the direction measured. In **Figure 1** we can see the two orthogonal planes of symmetry for a projection in Z direction:

- Perpendicular to spray direction: XY, coating top section, spherical splats.
- Parallel to spray direction: XZ and YZ (cross-section), here the splats are flattened.

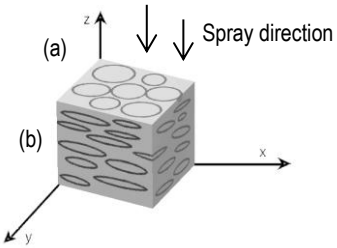

Figure 1: Representation of the two orthogonal planes of symmetry in a CGS projection. (a) XY plane, perpendicular to spray direction, and (b) XZ plane, following spray direction.

During CGS, as said before, high-velocity impact results in plastic deformation of the particles, leading to a compression and flattening in Z direction[15]. For this reason the microstructure analysis and mechanical properties obtained would be different when measured across axes in Z direction or in X and Y directions.

Not only spray direction influences on that effect but also the method used to throw the particles. There are many paths we can follow to obtain a bulk with different microstructure at each plane, from always repeating the same pattern to change the spray direction at each layer.

3.1.3. Advantages and disadvantages

To better understand the position of CGS in the field of AM, we have stated in **Table 1**[4] the main features of two other Metal Manufacturing Methods based on Powder Bed Fusion: Selective Laser Melting (SLM) and Selective Laser Sintering (SLS); and CGS which is based on

Metal Powder Application (MPA), in order to compare them and be able to see clearly pros and cons.

Table 1: Comparison of three AM processes: CGS, SLM and SLS.

	CGS or MPA	SLM	SLS
Process nature	Metal powder applied by kinetic compacting to build absolutely sealed materials with highly complex geometries.	To form three-dimensional solid parts by combining powder material with application of heat and pressure in an inert gas atmosphere.	Similar to SLM, to form three-dimensional solid parts by combining powder material with application of heat and pressure.
Principle	A thermal spraying process for metal powders in which material is uniformly dispersed, compacted and micro forging.	A layer powder melted on the bed with the help of high energy laser beam.	A layer of powder spread on the bed and selectively sintered by CO_2 laser in a two-dimensional cross section.
Technology	Thermal integrated with Metal Powder Application technology.	Layer by layer three-dimensional printing technology.	Layer by layer three-dimensional printing technology.
Advantages	- Complex materials can be manufactured. - Multiple materials can be fabricated simultaneously.	- High precision and high quality metal parts obtained. - Composites and ceramics can be also manufactured.	- Fast and accurate. - Superior surface finish. - Minimum material wastage.
Limitations	- High initial investment for equipment.	- Relatively new technology, high cost of machine and materials. - Inert gas supply required.	- Highly skilled operators required. - Cool down is near equal 50% of total manufacturing time. - Post processing required.
Unique features	Powder particles of 25 – 75μm grain size.	- Laser powder source range (100 – 1000 W). - Layer thickness 20μm.	- Precision range ±0.3%. - Minimum layer thickness of 0.08mm.

3.2. AM SUITABLE MATERIALS

Many materials are suitable for CGS technology from polymers to metals but in this project we have focused only on the latter: copper, aluminum, zinc, stainless steel, titanium, nickel and their alloys[16] are the most commonly used, due to their corrosion resistance and electrical and thermal conduction properties. In this experiment we are going to characterize more specifically 316L stainless steel.

3.2.1. 316L Stainless Steel

It is usual to add different elements to steel to obtain new products of Stainless Steel (SS) with desired properties and therefore get closer to new society and industry requirements[17]. **316 Marine-Grade SS** is perhaps one of the most widely known: it mainly consists by chrome and nickel forming an **austenitic** SS[18], meaning that it is non-magnetic and the amount of chrome goes from 16% to 26% and nickel is between 6% and 22%. It also has molybdenum in the range between 2% and 3%, which increases its corrosion and temperature resistance. There are many variants from 316 Grade. The most common are 316L, 316F, 316N and 316H; each is slightly different and used for different purposes.

316L SS has less carbon than 316 (that is why its name has an "L", from "low carbon") and it is generally made by manganese, chromium, nickel and molybdenum, that is the reason why as we have stated before, this material has special corrosion resistance (also to pitting corrosion) and strength at high temperatures, because lower carbon content minimizes deleterious carbide precipitation that weakens corrosion resistance. That is especially important when we use this material to weld because this carbon drowns out the metal, due to heat reacts with chromium weakening the corrosion resistance.

Some application areas of this material are[19]:

- Chemical and petrochemical processing (pressure vessels, tanks, heat exchangers, valves and pumps…)
- Food and beverage processing
- Marine
- Medical
- Petroleum processing
- Nuclear power generation
- Pulp and paper
- Textiles
- Water treatment
- Jet engine components

Therefore, we have used 316L SS as feedstock powder in CGS process to obtain a bulk and study its properties in different planes regarding the spray direction in order to see if anisotropic properties are present. In addition, we have treated thermally some samples to compare also between treated and non-treated CGS objects.

4. OBJECTIVES

The main objective of this project is to analyze CGS manufactured components of 316L SS comparing XY and XZ planes to know if they show anisotropy. For it, we have performed the following evaluations:

- Microstructure and porosity analysis
- Corrosion resistance evaluation
- Mechanical properties evaluation via tensile test and Vickers microhardness method

Finally, we will explore also the influence of a thermal treatment in anisotropic properties of CGS components.

5. EXPERIMENTAL SECTION

The following sections show the manufacturing process and previous characterization methods used to study the manufactured components microstructure, porosity, morphology, corrosion resistance and mechanical properties.

5.1. COMPONENTS MANUFACTURING

First of all, in order to assure a properly adhesion between the substrate and the sprayed powder, it is compulsory to get a high roughness surface. For that reason, we start **grinding** an aluminum substrate 10cm×10cm with alumina (aluminum oxide) until we obtain a surface as shown in **Figure 2**.

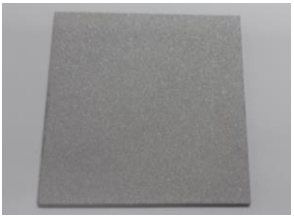

Figure 2: Aluminum substrate after pitting with alumina.

Secondly, we enter the set up data with the **parameters** (**Table 2**) for the bulk projection into the gun software. **Figure 3** shows the set up used in this project to perform the CGS manufacturing following the pattern of **Figure 4**.

Table 2: CGS selected parameters.

Parameters	Conditions
Propellant gas	N_2
Pressure of the gas	60 bar
Temperature of the gas	1000°C
Stand-off distance	20mm
Hatch distance	1mm
Layer number	70
Nozzle traverse speed	250mm/s
Spray steps	32

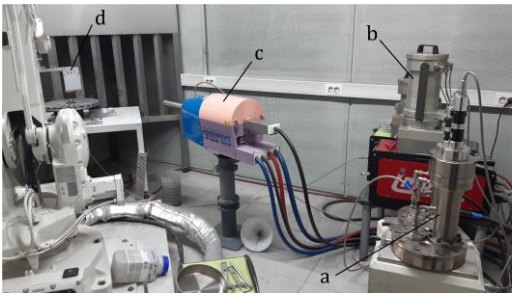

Figure 3: CGS set up at *Centro de Proyección Térmica* (CPT) Bio in *Bellvitge* used in the experiment. a) Powder feeder, b) Gas tank, c) De Laval type nozzle (spray gun), d) Substrate subjected in an articulated arm.

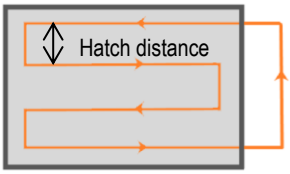

Figure 4: Pattern carried out in the experiment to manufacture our product by CGS and 316L SS.

The process lasted 37min approximately to obtain a 316L SS bulk of 7cm×6cm×2.4cm. If we take a clear look at the surface we notice that it is neither flat nor smooth since the path followed by the nozzle is apparent with parallel horizontal lines along (**Figure 5**), it is also remarkable the height difference between the both sides and the center (**Figure 6**) due to the turn that the nozzle has to do between lines.

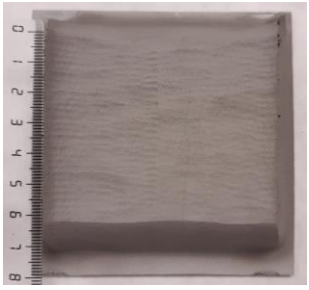

Figure 5: Surface sight of the CGS manufactured bulk.

Figure 6: Transversal sight of the CGS manufactured bulk.

In order to be able to perform microstructural characterization, corrosion evaluation and microhardness test, it is compulsory to reduce its size **cutting** it and keeping in mind the sections we want to examine (XY and XZ planes). As our bulk is resistant and heavy we have used the Abrasive Cutting Machine Abrasimet 250 for pieces that do not require a fine cut and the Abrasive blade 60A25 Struers Disk suitable for iron-based materials. **Figure 7** shows the final samples obtained after cutting.

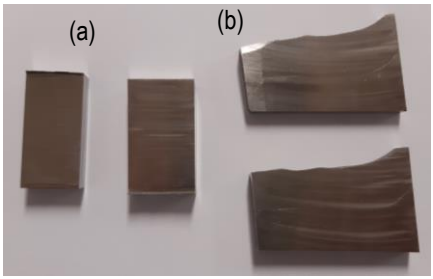

Figure 7: Samples obtained from cutting the CGS bulk. a) XY plane, and b) XZ plane.

5.2. THERMAL TREATMENT

We have also thermally treated two samples of each plane of interest cut previously to compare properties and microstructure of both treated and non-treated 316L SS manufactured by CGS. This thermal treatment consists of:

1) 30min heating from 100°C to 1000°C
2) 1h 1000°C
3) Normalization in standing air up to room temperature

5.3. METALLOGRAPHIC PREPARATION

In order to characterize metallurgic samples and study their physical structure it is compulsory to prepare its surface until flat and smooth[20]. As each material has his properties, each material needs different methods of grinding, polishing and etching for a perfect analysis via optical or electron microscopy[21;22]. **Table 3** shows the steps followed in this experiment to obtain the desired *mirror surface*.

Table 3: Metallographic preparation of CGS samples of 316L SS.

Stages	Steps
Grinding	1) Grit 120 (P120) 300rpm
	2) Grit 240 (P280) 300rpm 5min
	3) Grit 360 (P600) 300rpm 4min
	4) Grit 600 (P1200) 250rpm 3min
	5) P2500 250rpm 2min
Polishing	6) 6µm Di 250rpm 10min
	7) 1µm Di 250rpm 10min

Once the surface is well prepared in order to see the grain limits and the microstructure of the material we have attacked the surface sample with **Aqua Regia**, which consists of: 10ml of deionized water, 15ml of hydrochloric acid and 5ml of nitric acid.

5.4. CHARACTERIZATION METHODS

Once metallographic preparation of the materials is done, the samples are ready to analyze via microscopic techniques. The following paragraphs describe the techniques we have used in this project to characterize them.

5.4.1. Optical Microscopy

Optical Microscope (OM) is used in this experiment to study the **microstructure** as well as the **porosity** of our samples. In order to obtain clear images with differentiated grain limits and pores, we have attacked the samples with Aqua Regia.

The OM used in this study is *DM Leica 5000* available in CPT Business laboratory in the University of Barcelona (UB).

5.4.2. Scanning Electron Microscopy (SEM)

Electron microscopy uses a beam of highly energetic electrons produced after heating by current a tungsten wire. These electrons interact with the sample, which in turn promotes backscattered electrons, secondary electrons and X-rays. A detector gets their signal and after processing it, we are able to see a **three-dimensional image** of the sample in the screen

yielding us information about its **topography** and **morphology**. **Figure 8** displays the SEM used in the project, *JEOL JSM-5310* from CPT Business, and its main parts.

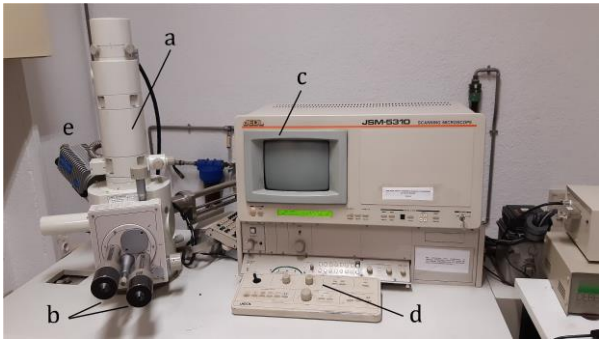

Figure 8: SEM used in the experiment from CPT Business. a) Electron column, b) Sample stage manual controls, c) Screen for menu and image display, d) Operation panels, and e) Vacuum system.

As said previously, the specimen also emits X-rays, but these ones are detected in a different detector allowing carrying out an **elemental analysis** since each element has its characteristic X-ray energy. In this analytical method called **Energy Dispersive X-Ray Spectroscopy** (EDS or EDX), we obtain a **spectrum** with the peaks correlated to the elemental composition of the specimen and an **elemental mapping**, which can be attractive to see clearly the elemental distribution in some sections. In this project we have done EDS after SEM, with *XFlash SVE III* from *Brucker Nano*.

5.4.3. X-Ray Diffraction (XRD)

In order to characterize 316L SS powder, XRD method has been used. It is based on Bragg's Law[23] and it consists of detecting X-Ray diffracted when X-ray beam is focused into a sample obtaining a **X-ray diffractogram** from which we can get information about **crystallographic structures** and **physical properties** of materials.

XRD data have been recorded with a Cu Kα radiation (λ = 1.5418Å) in a *PANalytical-X'Pert PRO MPD θ/ θ Bragg-Brentano* powder diffractometer available in *Centres Científics i Tecnològics de la UB* (CCiT UB). The analysis was carried out scanning from 5 to 100° 2θ with step size of 0.017°, measuring time of 100 seconds per step.

5.4.4. Dynamic Light Scattering (DLS)

This method is used for measuring the size and **size distribution** of molecules and particles by illuminating them with a laser and detecting from different angles the intensity of scattered light.

We have used this method to characterize powder size by using *LS 13 320 Multi-Wavelength Laser Diffraction Particle Size Analyzer* with Dry Tornado Module from *Beckman Coulter* available in CCiT UB.

5.4.5. Porosity

In order to quantify porosity in our samples and be able to compare them quantitatively, we have used ASTM (American Society for Testing and Materials) E2109-01(2014)[24] **image analysis** with the program *ImageJ*. It consists on editing an OM image of our sample surface to black and white and measure the balance of blacks in the area selected as representative elemental area (REA). This balance of blacks cannot be greater than a third part of total area. In the experiment it has been made ten replicates in order to obtain reliable results of porosity to compare properly the samples.

5.5. CORROSION RESISTANCE EVALUATION

Corrosion is the damage a material suffers due to the interaction with its environment; it consists of a chemical or **electrochemical reaction** involving an oxidation and a reduction. The metal surface is where the oxidation takes place (**anode**) since they usually have negative reduction potential, and depending on the environment composition the reduction can be the oxygen or the protons in solution (**cathode**). In our case, since SS is the metal (iron based) and the solution in contact with its surface is NaCl (3.5%), the reactions that take place would be the following:

- Anode: $Fe_{(s)} - 2\,e^- \leftrightarrow Fe^{2+}_{(aq)}$
- Cathode: $O_{2\,(g)} + 2H_2O_{(l)} + 4e^- \leftrightarrow 4OH^-_{(aq)}$

The set up used to do the measurements is shown in **Figure 9**. It is connected to a potentiostat *VSP-1 from* BioLogic which is controlled by using a computer with software EC-Lab.

The measurements have been performed at Electrodeposition and corrosion laboratory from *Secció de Química Física (UB).* As we can see, the cell has an only hole of **0.64cm²** where solution and sample make contact.

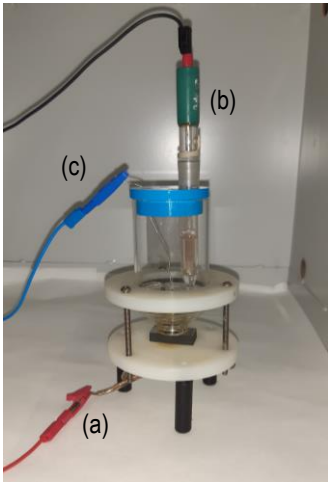

Figure 9: Corrosion cell used in the experiment in *Secció de Química Física UB*. a) Working electrode (316L SS), b) Reference electrode (Ag/AgCl/KCl 3.5M), and c) Auxiliary electrode (Pt).

First of all, we have put for 24 hours the sample in touch with the salt solution without applying any current and recording the potential until its variation was less than 5mV per hour. This way, we obtain the Corrosion Potential (E_{corr}), Equilibrium Potential (E_{eq}) or **Open Circuit Potential** (OCP, E_{OC}), required to perform the **Linear Polarization Resistance** (LPR), which consists of applying potential in the range of 5mV up and down from E_{OC} and plotting the intensity obtained in front of applied potential. The result is a linear representation from which we can obtain the polarization resistance (R_P) of the material without causing any damage on the sample surface. The parameters used in the experiment are summarized in **Table 4**.

Finally, we have done a **Potentiodynamic Polarization** (PP) or Polarization Curve by scanning the potential from lower values (cathodic) until higher values (anodic) from E_{OC} measuring current intensity in order to study both anodic and cathodic polarization curves that take place in our material. Therefore, adjusting Tafel slopes β_a (anodic curve) and β_c (cathodic curve) we obtain the Corrosion Potential (E_{corr}) and Corrosion current density (I_{corr}) in their intersection. Corrosion current density (j_{corr}) can be obtained in two different ways: from PP curve dividing the intensity by the area (equation **1**) or by using Stern-Geary equation (equation

2), which tends to be more accurate since it takes into account the polarization resistance from LPR performed previously and also Tafel slopes.

$$j_{corr} = \frac{I_{corr}}{S} = \frac{I_{corr}}{0.64} \quad (1)$$

$$j_{corr} = \frac{\beta_a \cdot |\beta_c|}{2.3 \cdot (\beta_a + |\beta_c|) \cdot R_P} \quad (2)$$

Table 4: Parameters used in the experiment to evaluate corrosion resistance of the samples.

OCP	LPR	PP
- 24h	- 2min	- 1h 30min
- dE_R/dt = 5mV/h	- E_{OC} ± 5mV	- E_{OC} + 600mV
	- 0.05mV/s	- E_{OC} – 250mV
		- 0.166mV/s

In order to register reliable results and conclusions, we have performed three replicates of each sample type as well as studied their surface composition and topography after the test.

5.6. MECHANICAL PROPERTIES

5.6.1. Tensile test

Another aspect to analyze is the mechanical properties of the sample obtained. For this reason it has been manufactured another bulk and cut in three different planes (X, Y, Z) to obtain **bone shape samples** such as in **Figure 10** to perform our **tensile test** with *ZMART.PRO* device from *Zwik/Roell* found in the *Departament de Ciència de Materials* (UB).

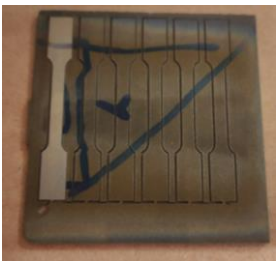

Figure 10: Bone shape samples manufactured to perform a tensile test and study the mechanical properties of 316L SS made by CGS.

It consists on holding the sample from both sides (which are wider) and pull with clamping jaws until sample rupture. After plotting **stress** (equation 3) according to percentage of **strain** or deformation (equation 4) we are able to know the point at which the material fails as well as its modulus of elasticity, strain and yield strength.

$$\sigma = \frac{F}{S_0} = \frac{Applied\ Force}{Area\ perpendicular\ to\ the\ force\ direction} \quad (3)$$

$$\%\varepsilon = \frac{\Delta l}{l_0} \cdot 100 = \frac{clamping\ jaw\ displacement\ percentage}{initial\ clamping\ jaw\ position} \quad (4)$$

The dimensions of our bone shape samples are represented in **Figure 11**.

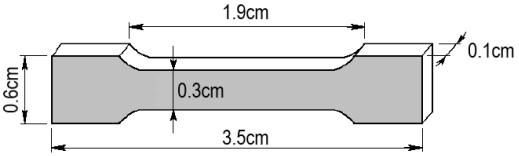

Figure 11: Bone shape samples dimensions.

5.6.2. Vickers microhardness test

Finally, we are going to use MXT-α MATSUZAWA from CPT Business to perform **Vickers microhardness test method** to evaluate the surface resistance to indentation of the four CGS sample types by following ASTM standard C1327-15 (2019)[25] since we have small samples. It consists of applying a load (50g in our case) with a diamond indenter in the form of a right pyramid with a square base having an angle of 136° between the opposite faces, to a smooth and well-polished area. Measuring the resulting length of the diagonals of the rhombus indentation (**Figure 12**) we can obtain a hardness value by using equation 5.

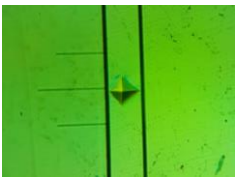

Figure 12: Vickers Hardness indentation image.

$$HV = 0.102 \cdot \frac{F}{S} = 0.102 \cdot \frac{2F \sin\frac{\theta}{2}}{d^2} = 0.1891 \cdot \frac{F}{d^2} \quad (5)$$

6. RESULTS AND DISCUSSION

6.1. POWDER CHARACTERIZATION

First of all, we are going to introduce and discuss the feedstock powder 316L SS used in this project to perform CGS additive manufacturing.

6.1.1. Microstructure

In order to characterize 316L SS powder morphology we have used SEM. **Figure 13** and **Figure 14** show its three-dimensional appearance at different magnification. We notice an **irregular** morphology and different sizes between particles since this powder has been performed by water atomizing. This powder manufacturing method consists of spraying the material in liquid phase with high pressure water to obtain drops of the metal that solidify quickly.

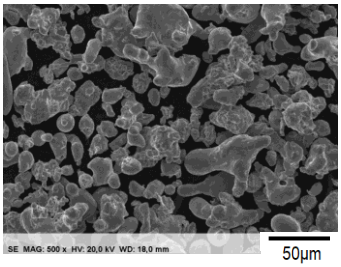

Figure 13: SEM 316L SS powder three-dimensional image x500 magnification.

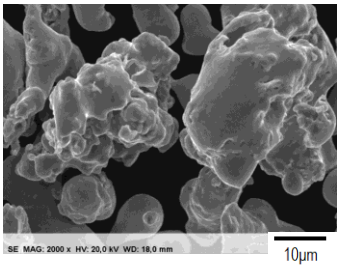

Figure 14: SEM 316L SS powder three-dimensional image x2000 magnification.

Another aspect that has been analyzed is the cross section, that is, the microstructure of our powder. In **Figure 15** and **Figure 16** we can see that it has not a smooth surface since it has **dendrites**, visible due to the difference in brightness. They are common in alloys because of the manufacturing process; since our powder is cooled down quickly by water atomizing, the number of nucleus increase leading to small dendrites visible via optical microscopy.

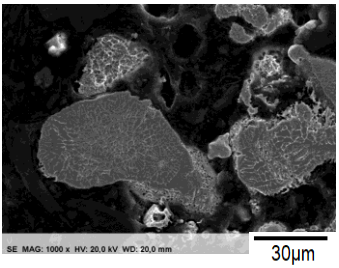

Figure 15: SEM 316L SS powder cross section x1000 magnification.

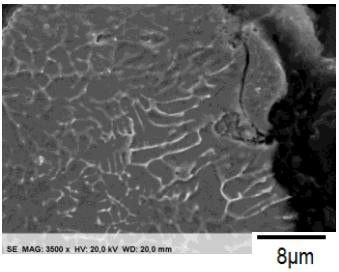

Figure 16: SEM 316L SS powder cross section x3500 magnification.

6.1.2. Elemental composition

After EDS quantification in different areas of the powder, we have obtained the values summarized in **Table 5** with the standard deviation. As expected **Fe**, **Cr** and **Ni** are the predominant elements with values near the stated ranges for 316L SS (*reference 316L SS* in **Table 5**).

Table 5: 316L SS powder quantification after SEM+EDS.

Detected elements	Mean (%)	Standard Deviation (%)	Reference 316L SS[19] (%)
Fe	Balance	-	Balance
Cr	14.85	1.06	16-18
Ni	13.77	1.47	10-14
Mo	3.23	1.04	2-3
Mn	2.45	0.19	2
Si	0.94	0.47	0.75

6.1.3. Crystallographic structure

The diffractogram obtained from XRD shows, as expected, how 316L SS powder crystallographic structure basically corresponds to **austenite** and a minimum part of martensite since as said before, this material is principally austenitic. In **Figure 17** we can see the identification of the main picks of both crystallographic structures.

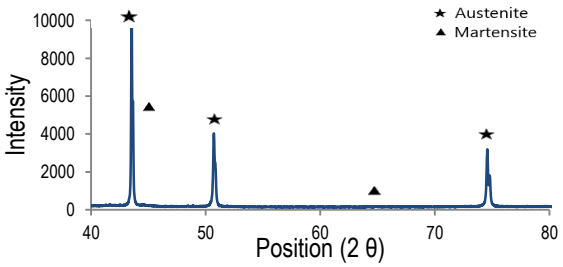

Figure 17: XRD diffractogram of 316L SS powder.

6.1.4. Particle Size Distribution

To know the Particle Size Distribution (PSD) of our powder, DLS provides two in one graph representing differential volume (%) and cumulative volume (%) according to particle diameter (μm). They differ from one another only in the fact that cumulative volume is the integration of differential volume. If we take a clear look at **Figure 18** we can obtain three interesting data from this integration: d10, d50 and d90, since the three numbers are related to cumulative volume. The PSD obtained in the powder is the following:

- Median or d50 = **31.58 μm**
- d10 = 15.58 μm
- d90 = 60.03 μm

Therefore, particles below 15.58 μm of diameter are the 10% of the total powder volume, those below 31.58 μm the 50%, and those below 60.03 μm the 90%. Taking into account that the suitable range in CGS depositions is between 20 and 49 μm[26] we consider an appropriate powder for our process.

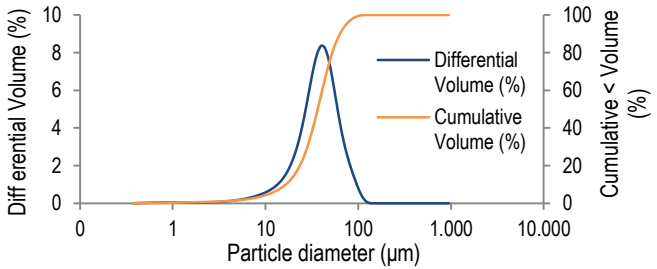

Figure 18: Differential and cumulative volume (%) of 316L SS powder.

6.2. BULK CHARACTERIZATION

The following sections discuss the main properties analyzed in this project of the different manufactured samples made by CGS: microstructure, porosity, corrosion resistance and mechanical properties such as tensile test and microhardness.

6.2.1. Microstructure

In **Figure 19** we can see the four types of sample studied in this project. If we start describing the image related to XY plane, perpendicular to the nozzle direction, the particles are rounded of different sizes; then, if we look at the XZ plane, which is parallel to the spray direction, here the particles are not spherical but flattened. This is due to CGS bonding mechanism described previously, since XZ plane reveals plastic deformation suffered in the process by the sprayed particles unlike XY plane. Therefore, it is confirmed certain anisotropy in our additive manufactured 316L SS bulk since XY and XZ planes present different microstructures.

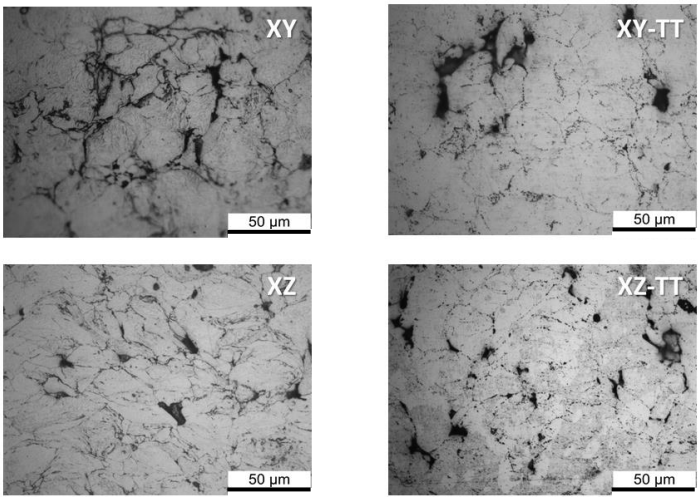

Figure 19: OM images of the four sample types studied in the experiment at x50 magnification: XY plane; XY plane-Thermally Treated; XZ plane; and XZ plane-Thermally Treated.

The right-hand side of **Figure 19** corresponds to Thermally Treated (TT) samples. As expected, particle limits are less visible now and particle surfaces are flatter and more homogeneous than non-treated samples. Thus, thermal treatments influence on the material microstructure bringing uniformity on both planes of the studied compound. That is related to the

fact that bringing the material up to 1000° increases diffusion effect through particle limits and therefore chemical bonding between them.

6.2.2. Porosity

Table 6 summarizes the porosity values obtained after image analysis of the samples surface with the standard deviation. It is divided into three different areas of study due to the fact that the parallel to the spray direction plane (XZ) can provide information about how compaction changes along the process.

If we focus on XZ samples the percentage of porosity is significantly higher in the middle area since they present a central vein crossing the plane due to an error in the manufacturing process, for this reason we are not taking into account quantitatively. If we take a look to the values measured for the area near the substrate (labeled as *down area* in **Table 6**) we notice that they are lower (1.99%) than the top area of the component (labeled as *up area* in **Table 6**) porosity (3.61%). This fact makes sense since these particles experience more compaction as it is an AM process and solid particles continuous impact promotes the compression of the first deposited layers. Therefore, porosity cannot be considered equal along the parallel direction of projection.

Moving on to XY plane, it only shows a porosity value (3.83%) because it does not present any heterogeneity unlike the previous. If we compare it with the XZ plane described previously, we can see how close XY porosity is with the XZ top area porosity, this agrees with the fact that the lower porosity value in XZ *down area* is due to compaction of the upper impacted particles.

Finally, if we take a look at the variation from non-treated to TT samples it is clear the downward trend in porosity when samples are TT since heat treatment promotes the material diffusion between particle limits decreasing pores percentage. This fact agrees with the microstructure characterization described above that showed a more homogeneous surface with less pores.

Table 6: Porosity values and standard deviation of the four sample types studied.

Studied area	Up (% area)	Middle (% area)	Down (% area)
XY	-	3.83 ± 1.13	-
XY-TT	-	1.59 ± 0.94	-
XZ	3.61 ± 1.01	12.71 ± 1.08	1.99 ± 1.51
XZ-TT	0.47 ± 0.21	2.77 ± 1.24	0.35 ± 0.05

6.3. CORROSION RESISTANCE EVALUATION

Figure 20 represents the five PP curves obtained after scanning from cathodic to anodic domain for each sample type. The main peak observed in these typical curves is related to the equilibrium between these two zones, therefore we can obtain the corrosion potential and corrosion rate in this point. For that, we need to adjust both Tafel slopes from anodic (β_a) and cathodic (β_c) curves as in **Figure 21**.

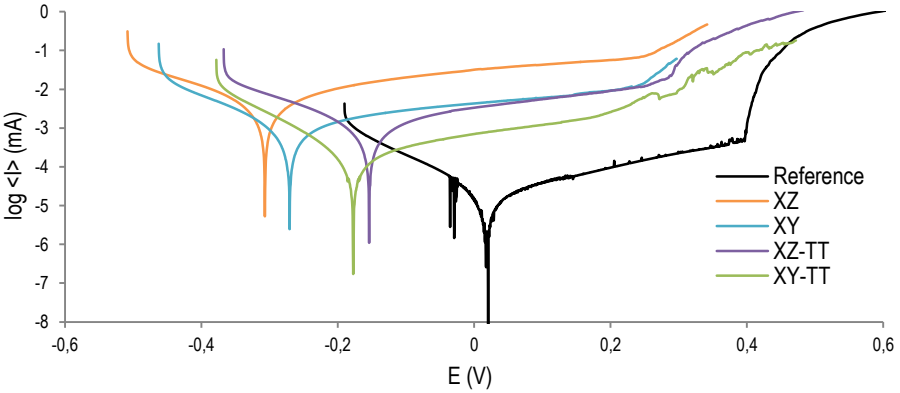

Figure 20: PP curve of the four CGS samples and 316L SS reference.

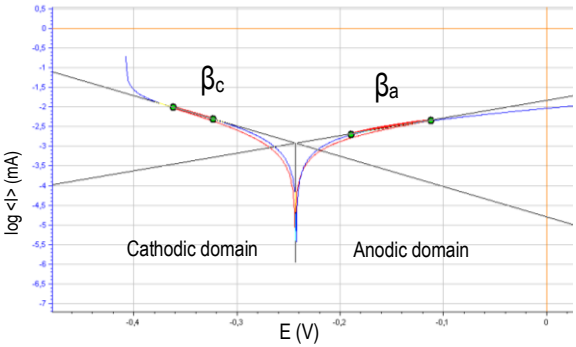

Figure 21: Representation of corrosion potential obtention by adjusting Tafel slopes.

Furthermore, it has been performed three replicates of each sample in order to obtain more reliable results of corrosion resistance properties. The reference material used in this evaluation is a bulk 316L SS plate. If we start comparing it with the rest of the samples we notice that its

corrosion potential is higher and greater than zero. It also has low corrosion rate (j_{corr}) and consequently high Polarization Resistance (Rp) (equation **2**).

If we take a look at non-treated samples we notice that XZ plane is the one that appears furthest to the left side in **Figure 20**, this is related to the fact that its corrosion potential is the more negative (-307mV) and also its corrosion intensity is high, which means that it is easily oxidized. These facts can be related with the previous characterization; since it has shown high levels of porosity and for hence, its corrosion resistance is lower. Moving on to XY plane, it is not far from XZ but its PP curve is slightly nearer to the reference, with higher polarization resistance. We can also associate this variation between both planes to microstructure properties and porosity values described before. Therefore, it is confirmed differences in the corrosion resistance between these two perpendicular planes.

At the right hand of non-treated samples there are the PP curves of the TT samples. Thus, they show higher corrosion resistance since their corrosion intensities are lower and they are closer to the reference; moreover, both planes behave more similar. Then, it is concluded that anisotropy loses strength when CGS components are TT, which makes sense since treating thermally the samples decrease porosity percentages and homogenize the microstructure as we have seen above; that is why corrosion resistance is also improved.

The main results obtained from this corrosion resistance evaluation and their standard deviations are summarized in **Table 7**. If we focus here on the corrosion rate obtained by the two different ways described previously: by using Tafel current intensity from the PP curve (equation **1**), and from Stern-Geary Equation (equation **2**) taking into account the polarization resistance and Tafel slopes; we notice that we obtain almost the same values. This fact shows that the method has been performed successfully.

Table 7: Corrosion resistance evaluation of the five type samples of 316L SS.

	Rp ($k\Omega/cm^2$)	E_{corr} (mV)	β_c (mV/dec)	β_a (mV/dec)	j_{corr} (Stern-Geary) ($\mu A/cm^2$)	j_{corr} (Tafel) ($\mu A/cm^2$)
316L SS ref.	1136±449	24±7	103±15	227±59	0.030±0.017	0.023±0.012
XZ	5±3	-307±1	147±50	199±68	8.07±2.46	6.05±0.06
XY	25±16	-257±19	129±2	232±12	1.79±1.11	1.51±0.51
XZ-TT	17±8	-203±84	164±11	237±43	2.83±1.35	2.33±0.75
XY-TT	160±51	-189±16	107±1	269±17	0.22±0.06	0.29±0.03

6.3.1. Visual analysis after corrosion test

Another aspect to take into account is the appearance of the samples once corrosion evaluation is done. It has been significant differences between non-treated and TT samples. The last ones have been kept still smooth with any visible defect with naked eye, whereas non-treated samples have shown darker zones on its surface due to the metal oxidation.

Therefore, the area where the corrosion tests have been carried out was inspected by SEM (**Appendix 1**) in order to know more about the corrosion effect in our samples.

In these images it has been observed that SS corrosion mainly occurs in the limit between particles. These regions are the preferential paths for corrosive agent to move through the sample, entering by the surface irregularities such as pores. This fact explains the poorest corrosion resistance shown by the sample corresponding to XZ plane since it showed high levels of porosity, which accelerates corrosion on its surface.

Finally, new precipitates on these remarkable areas have been quantified by EDS. As expected some samples have Na or Cl on its surface since the electrode solution is NaCl 3.5%. But main areas only have Cl, which suggests that new chlorides compounds have been formed (usually, corrosion products are hydroxychlorides or hydroxycarbonates). Other elements that appeared are O and C.

6.4. MECHANICAL PROPERTIES

6.4.1. Mechanical resistance

In order to know the mechanical resistance of the CGS bulk it has been tested X, Y and Z directions of another CGS manufactured bulk and also after thermally treating it. **Figure 22** shows the characteristic Stress-Strain curves from the tensile test process until rupture of five samples performed. These kinds of curves give us information about the rigidity in each case since stress is the load applied to the bone shape sample and the percentage of strain is the deformation or elongation experienced by this sample until break. The first part of the curve is related to elastic deformation, atoms displaced recover their position once stress is removed, this area is lineal and its slope represents the rigidity of the material known as Young's Modulus, after that, plastic deformation takes place and atoms cannot return to their initial positions once the effort is removed, this area uses to be more large and stable and goes just before the rupture point.

The most distinguished difference in **Figure 22** is between non-treated and TT samples, it is clear to see how TT curves are larger since they experience plastic deformation, whereas non-treated samples break in the elastic zone. Therefore, they have improved significantly theirs mechanical properties after the thermal treatment supporting higher stress until fracture. Another aspect observed is the homogenization of the results for the three sample types since they support the same stress if we consider standard deviations, that is consistent with corrosion evaluation performed above, which affirms anisotropic properties loss when CGS components are TT.

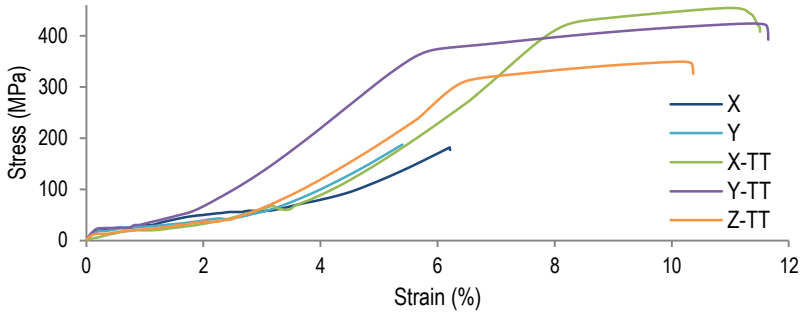

Figure 22: Stress-Strain curves obtained from tensile tests of five CGS samples.

Table 8 summarizes the values of stress and strain in the Ultimate Tensile Strength (UTS) for each sample as well as the standard deviation obtained after three replicates.

If we take a look to Z direction samples results, we notice that they have broken after applying the lowest stress and also with the highest percentage of strain; this is due to the fact that, as stated previously, it does not experience plastic deformation. Low rigidity results for this direction samples are related to the previously XZ plane, which has been also the one with higher porosity and lower corrosion resistance. If we know that this direction is perpendicular to the nozzle direction and it is composed by the connections between the layers of the bulk, the results obtained lead us to the conclusion that these connections are not as strong as the others in this manufacturing.

Directions X and Y have better values than Z direction since they have higher stress with lower strain percentage when break; therefore, it is confirmed anisotropy between Z and X, Y directions. If we focus on X and Y directions numbers both directions have practically the same UTS, this fact can be explained since they form two orthogonal planes of symmetry (XZ and YZ)

in CGS manufactured components (**Figure 1**). This has been taken into account to perform the analysis in this experiment by only testing XZ plane and considering equal results for YZ plane.

Table 8: UTS and strain values measured in the tensile tests for the different CGS samples with their standard deviation.

	Tensile strength (MPa)	Strain (%)
X	173.63 ± 8.62	4.79 ± 0.26
Y	183.93±39.46	4.70 ± 0.51
Z	86.30 ± 21.84	4.86 ± 0.73
X-TT	422.37 ± 12.40	7.23 ± 0.96
Y-TT	409.34 ± 47.93	7.91 ± 0.52
Z-TT	430.62 ± 13.45	7.49 ± 0.31

In order to better understand the previous results we have analyzed via SEM the fracture surface after tensile test (**Appendix 2**). The images show significant differences between non-treated and TT samples rupture microstructure. The first one is partially smooth as if entire particles were isolated (fragile fracture), this fact is due to they break in grain limits since these connections are the weakest areas. By contrast, TT samples seem to have more plastic deformation during the tensile test until breaking because of they show a regular microstructure with plastically deformed peaks, which may be correspond to the ductile fracture of the component. This result agrees with the results of the tensile tests (**Figure 22**), since the TT samples show larger curves with elastic and plastic deformation.

6.4.2. Microhardness

The last assay performed has been Vickers microhardness test in order to know more about hardness properties of compounds made by CGS. The results obtained are in **Figure 23** with its standard deviation after 10 tests.

If we focus on non-treated planes we notice that as expected, XY plane is harder than XZ. This fact fits with the previous results in which we have seen how XZ plane samples have a microstructure where particles do not connect as well as in XY plane.

After TT, TT samples show lower microhardness values because of the treatment relaxes stress areas between particles which decreases its hardness properties. In addition, for both planes the high standard deviation values obtained for the sample without TT decrease after heat treatment because of the homogenization of the surface as we have seen in many characterizations in this project.

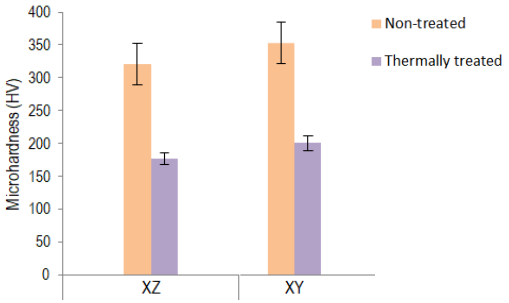

Figure 23: Vickers hardness and standard deviations of the four sample types studied.

7. CONCLUSIONS

The conclusions obtained after analyzing CGS 316L SS components properties according to the observation plane via different methodologies are the following:

- Microstructural analysis and porosity characterization show differences between planes XY and XZ, with higher percentage of porosity in the parallel plane to the spray direction.
- CGS components have more negative corrosion potential and lower corrosion resistance than 316L SS manufactured in the conventional way. Corrosion resistance of XY plane is higher than XZ.
- Z direction sample resists less stress than X and Y directions after performing the tensile test, although strain percentages of the three sample types are very similar. Microhardness for XY plane is higher than for XZ plan.

Then, it has been concluded the presence of anisotropic properties in these kinds of components. Furthermore, after thermally treating the samples all these differences disappear since X, Y and Z directions and XZ, XY planes obtain almost indistinguishable properties studied. It is therefore concluded that anisotropic properties disappear when CGS 316L SS samples are TT.

8. REFERENCES AND NOTES

(1) Molitch-Hou, M. Overview of Additive Manufacturing Process. In *Additive Manufacturing: Materials, Processes, Quantifications and Applications*; Elsevier, **2018**; 1–38.

(2) Peng, T.; Zhu, Y.; Leu, M.; Bourell, D. Additive Manufacturing-Enabled Design, Manufacturing, and Lifecycle Performance. *Addit. Manuf.* **2020**, *36*, 101646.

(3) Zenou, M.; Grainger, L. Additive Manufacturing of Metallic Materials. In *Additive Manufacturing: Materials, Processes, Quantifications and Applications*; Elsevier, **2018**; 53–103.

(4) Pratheesh Kumar, S.; Elangovan, S.; Mohanraj, R.; Ramakrishna, J. R. Review on the Evolution and Technology of State-of-the-Art Metal Additive Manufacturing Processes. *Mater. Today Proc.* **2021**.

(5) Cooke, S.; Ahmadi, K.; Willerth, S.; Herring, R. Metal Additive Manufacturing: Technology, Metallurgy and Modelling. *J. Manuf. Process.* **2020**, *57*, 978–1003.

(6) Ang, A. S. M.; Berndt, C. C. A Review of Testing Methods for Thermal Spray Coatings. *Int. Mater. Rev.* **2014**, *59* (4), 179–223.

(7) Darut, G.; Dieu, S.; Schnuriger, B.; Vignes, A.; Morgeneyer, M.; Lezzier, F.; Devestel, F.; Vion, A.; Berguery, C.; Roquette, J.; Le Bihan, O. State of the Art of Particle Emissions in Thermal Spraying and Other High Energy Processes Based on Metal Powders, ScienceDirect. *J. Clean. Prod.* **2021**, *303*, 126952.

(8) Klassen, T.; Gärtner, F.; Schmidt, T.; Kliemann, J. O.; Onizawa, K.; Donner, K. R.; Gutzmann, H.; Binder, K.; Kreye, H. Basic Principles and Application Potentials of Cold Gas Spraying. *Materwiss. Werksttech.* **2010**, *41* (7), 575–584.

(9) Guilemany, J. M.; Dosta, S.; Garcia, I.; Concustell, A.; Cinca, N. Cold Gas Spray: Innovative Technology in Surface Engineering. **2014**.

(10) Li, C. J.; Li, W. Y.; Liao, H. Examination of the Critical Velocity for Deposition of Particles in Cold Spraying. *J. Therm. Spray Technol.* **2006**, *15* (2), 212–222.

(11) Li, W.-Y.; Zhang, C.; Guo, X. P.; Zhang, G.; Liao, H. L.; Li, C.-J.; Coddet, C. Effect of Standoff Distance on Coating Deposition Characteristics in Cold Spraying. *Mater. Des.* **2008**, *29* (2), 297–304.

(12) Grujicic, M.; Zhao, C. L.; DeRosset, W. S.; Helfritch, D. Adiabatic Shear Instability Based Mechanism for Particles/Substrate Bonding in the Cold-Gas Dynamic-Spray Process. *Mater. Des.* **2004**, *25* (8), 681–688.

(13) Bae, G.; Xiong, Y.; Kumar, S.; Kang, K.; Lee, C. General Aspects of Interface Bonding in Kinetic Sprayed Coatings. *Acta Mater.* **2008**, *56* (17), 4858–4868.

(14) A. Papyrin , V. Kosarev, S. Klinkov, A. Alkhimov, V. F. Discovery of the Cold Spray Phenomenon and Its Basic Features. *Cold Spray Technol.* **2007**, *1*, 1980.

(15) Yin, S.; Jenkins, R.; Yan, X.; Lupoi, R. Microstructure and Mechanical Anisotropy of Additively Manufactured Cold Spray Copper Deposits. *Mater. Sci. Eng. A* **2018**, *734*, 67–76.

(16) Benedetti, A. V.; Santos da Silva, F; Cinca, N.; Dosta, S.; Garcia, I.; Guilemany, J. M. Cold Gas Spray Coatings: Basic Principles, Corrosion Protection and Applications. *Eclética Química* **2017**, *42*, 9–32.

(17) ¿Cuáles son las propiedades del acero inoxidable 316 y 316L?,

https://jnaceros.com.pe/blog/propiedades-acero-inoxidable-316-316l/ (accessed Mar 7, 2021).
(18) Bell, T. Type 316 and 316L Stainless Steels, https://www.thoughtco.com/type-316-and-316l-stainless-steel-2340262 (accessed Mar 7, 2021).
(19) Aleación 316-316L, https://www.sandmeyersteel.com/spanish/316-316L.html (accessed Mar 7, 2021).
(20) Metallographic Specimen Preparation, https://www.kemet.co.uk/blog/metallography/metallographic-specimen-preparation (accessed Mar 13, 2021).
(21) Song, B.; Wen, S.; Yan, C.; Wei, Q.; Shi, Y. Materials Characterization. In *Selective Laser Melting for Metal and Metal Matrix Composites*; Elsevier, **2021**; pp 231–247.
(22) What is Metallography?, https://www.kemet.co.uk/blog/metallography/what-is-metallography (accessed Mar 21, 2021).
(23) X-ray Powder Diffraction (XRD), https://serc.carleton.edu/research_education/geochemsheets/techniques/XRD.html (acessed May 12, 2021).
(24) ASTM E2109 – 01, Standard Test Methods for Determining Area Percentage Porosity in Thermal Sprayed Coatings, *ASTM International*, **2014**.
(25) ASTM C1327 - 15, Standard Test Method for Vickers Indentation Hardness of Advanced Ceramics, *ASTM International*, **2019**.
(26) Wong, W.; Vo, P.; Irissou, E.; Ryabinin, A. N.; Legoux, J. G.; Yue, S. Effect of Particle Morphology and Size Distribution on Cold-Sprayed Pure Titanium Coatings. *J. Therm. Spray Technol.* **2013**, *22* (7), 1140–1153.

9. ACRONYMS

ASTM: American Society for Testing and Materials

CCiT: Centres Científics i Tecnològics

CGS: Cold Gas Spray

CPT: Centro de Proyección Térmica (*Thermal Spray Center*)

DLS: Dynamic Light Scattering

EDX or EDS: Energy Dispersive X-Ray Spectroscopy

LPR: Linear Polarization Resistance

MPA: Metal Powder Application

OCP: Open Circuit Potential

OM: Optical Microscopy

PP: Potentiodynamic Polarization

PSD: Particle Size Distribution

SEM: Scanning Electron Microscopy

SLM: Selective Laser Melting

SLS: Selective Laser Sintering

SS: Stainless Steel

TT: Thermally Treated

UTS: Ultimate Tensile Strength

XRD: X-Ray Diffraction

APPENDICES

APPENDIX 1: SEM AFTER CORROSION TEST

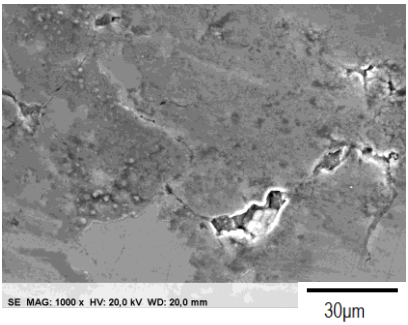

Figure 1.1: XY plane SEM x1000 magnification.

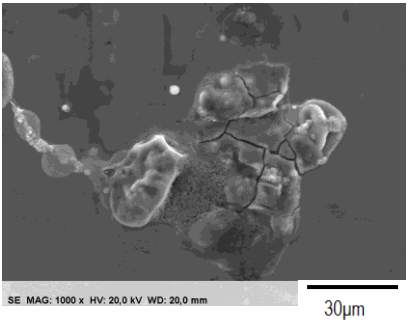

Figure 1.2: XZ plane SEM x1000 magnification.

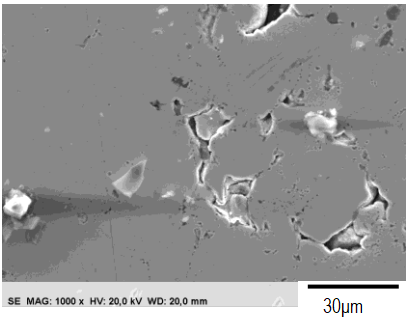

Figure 1.3: XY plane TT SEM x1000 magnification.

APPENDIX 2: SEM ANALYSIS OF THE FRACTURE SURFACE OF TENSILE TEST SAMPLES

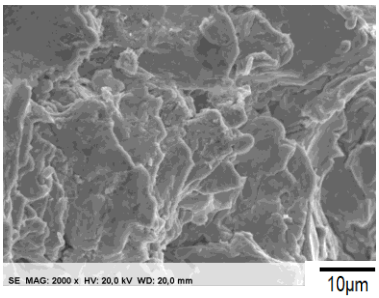

Figure 2.1: X direction sample rupture microstructure SEM image x2000 magnification.

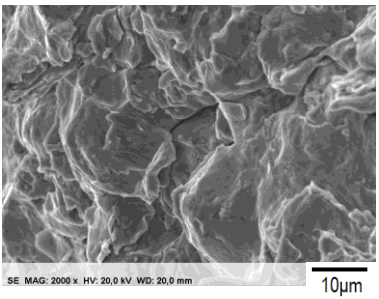

Figure 2.3: Z direction sample rupture microstructure SEM image x2000 magnification.

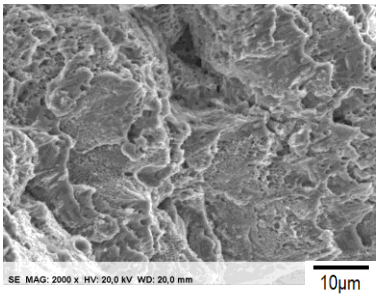

Figure 2.2: X direction TT sample rupture microstructure SEM image x2000 magnification.

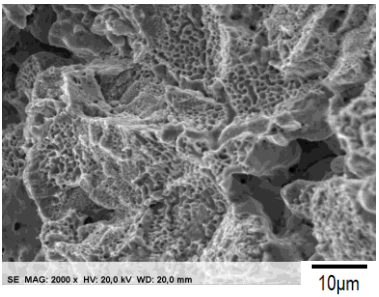

Figure 2.4: Z direction TT sample rupture microstructure SEM image x2000 magnification.